Materials Research Proceedings 41 (2024) 1353-1362 https://doi.org/10.21741/9781644903131-150

In-process tool pose measurement in incremental sheet forming

TERLAU Marina[1,a *], VON FREYBERG Axel[1,b] and FISCHER Andreas[1,c]

[1]University of Bremen, Bremen Institute for Metrology, Automation and Quality Science, Linzer Straße 13, 28359 Bremen, Germany

[a]m.terlau@bimaq.de, [b]a.freyberg@bimaq.de, [c]andreas.fischer@bimaq.de

Keywords: Incremental Sheet Forming, Tool Pose Measurement, Shadow Imaging

Abstract. Robotic incremental sheet forming is flexible, but involves significant forming path deviations, demanding an in-process tool pose measuring system. To achieve a 50 µm positional and 0.05° orientational measuring uncertainty, a triangulation system using multiple shadow imaging sensors is proposed. LEDs with different wavelengths are attached to the tool holder and cast a shadow of the sensor's mask though a color filter on the camera chip behind it. The LED position is obtained by processing the shadow images of at least two sensors. Conducted experiments demonstrate that the filters effectively separate the shadows, ensuring cross-sensitivities as low as the random error of measuring a single LED position. The unpredictable scatter in the systematic error dominates the LED position measurement uncertainty. However, a Monte Carlo simulation shows the feasibility of achieving the required uncertainty for tool pose measurement.

Introduction

Robotic incremental sheet forming (ISF) offers a cost-effective alternative for producing large sheet metal components in limited quantities [1]. However, the robot's low stiffness causes load-induced deformations, leading to significant path deviations [2]. Accurate tool pose prediction is challenging due to dynamic manufacturing conditions [3]. Thus, in-process tool pose measurement is preferred. To cover deviations along the kinematic chain, a direct contactless measurement is needed, which is independent of the robot kinematics and enables real-time compensation.

To achieve the fast and contactless in-process measurement of the 6-DOF tool pose, i. e. position and orientation, an optical measurement system is demanded, which works in single shot, is able to cover the machining volume of 1.0 m × 1.0 m × 0.2 m, and provides a sufficient measurement uncertainty of position and orientation of 50 µm and 0.05°, respectively.

During robot calibration the end-effector pose was measured by laser trackers [4], but they determined the tool orientation not in a single shot. Applying photogrammetry, robot end-effectors were tracked and controlled [5, 6]. The robot joint stiffness model was determined using 3D digital image correlation [7]. Although camera based methods cover a large measurement volume in a single shot with low measurement uncertainties [8], usually costly high-resolution cameras are required. This leads to high data amount which complicates real-time path correction. Additionally, the information in the image is spread over just a few pixels.

To increase the information content, shadow imaging introduced by Grenet et al. [9] is proposed for tool pose measurement. Thereby, the position of a light source is measured from the shadow, which the light source produces on a camera chip by passing through a mask. Analyzing the shadow images gives the direction to the light source, and triangulating the directions of at least two sensors provides the light source position. Studies confirm the capability to detect the 3D position of one light source [10]. However, the simultaneous measurement of at least three light source positions is necessary to calculate the tool pose. Therefore it needs to be clarified, in what extent shadow imaging sensors are capable of extracting each single light source position, how

large is the cross-influence of the different light source channels, and what is the resulting achievable measurement uncertainty of the 6-DOF tool pose.

Hence, the aim of this article is to assess the capability of shadow imaging for measuring the 6D tool pose during robotic ISF. In this context, the cross-sensitivities between different light sources are investigated and combined with the examined uncertainty of the LED position. Finally, the tool pose measurement uncertainty is evaluated using a Monte Carlo simulation.

For this purpose, the principle of the tool pose measurement by determining the positions of three light sources is introduced first. The experimental setups, investigating the uncertainty in light source position measurement and cross-sensitivities among the light sources is addressed, and the outcomes from these investigations are subsequently presented and discussed. Lastly, a conclusion and future perspectives are provided.

Measuring Principle

Light source position measurement.

For tool pose measurement, the several light source positions are measured separately but simultaneously. To measure a single light source position utilizing the shadow imaging principle, multiple sensors are employed for the 3D position measurement. In each sensor, the light source creates a shadow of a mask on a camera chip. From the shadow position extracted by image processing, each sensor $n = 1 \dots N$ provides a direction $\boldsymbol{r}_{\mathrm{M},n}$ to the light source. Together with the sensor positions $\boldsymbol{s}_n$ (known from the calibration, also in the machine coordinate system (MCS) M), the lines from each sensor to the light source position are obtained as $\boldsymbol{s}_n + t_n \cdot \boldsymbol{r}_{\mathrm{M},n}$ with t_n as function variable. In the ideal case, all lines intersect at the sought-after position of the light source. In real 3D measurements, the lines from the sensors do not intersect at a single point, so that the light source position is determined from the point $\hat{\boldsymbol{l}}_{\mathrm{M}}$ that is closest to all lines (least summed squared distances):

$$\min_{\boldsymbol{l}_{\mathrm{M}}} \left(\sum_{n=1}^{N} \left(\frac{\left| (\boldsymbol{l}_{\mathrm{M}} - \boldsymbol{s}_n) \times \boldsymbol{r}_{\mathrm{M},n} \right|}{\left| \boldsymbol{r}_{\mathrm{M},n} \right|} \right)^2 \right). \tag{1}$$

The direction vector $\boldsymbol{r}_{\mathrm{M},n}$ in the MCS is obtained by a coordinate transformation of the detected direction vector $r_{\mathrm{S},n}$ in the sensor coordinate system S. This transformation is performed by applying a rotation matrix $R_{\mathrm{MS},n}$, which is obtained from the sensor's calibration:

$$\boldsymbol{r}_{\mathrm{M},n} = \boldsymbol{R}_{\mathrm{MS},n} \cdot \boldsymbol{r}_{\mathrm{S},n}. \tag{2}$$

Note that any potential misalignment between the mask and the camera is reduced during the sensor setup and thus disregarded. According to Fig. 1, the vector $\boldsymbol{r}_{\mathrm{S},n}$ follows from the shadow position $(\xi_{\mathrm{i},n}, \zeta_{\mathrm{i},n})$ on the camera chip, the calibrated distance h_n between mask and camera chip, and the known reference shadow position $(\xi_{\mathrm{i},0,n}, \zeta_{\mathrm{i},0,n})$ where the light source is centered in front of the camera:

$$\boldsymbol{r}_{\mathrm{S},n} = \begin{bmatrix} \xi_{\mathrm{i},0,n} - \xi_{\mathrm{i},n} \\ h_n \\ \zeta_{\mathrm{i},0,n} - \zeta_{\mathrm{i},n} \end{bmatrix}. \tag{3}$$

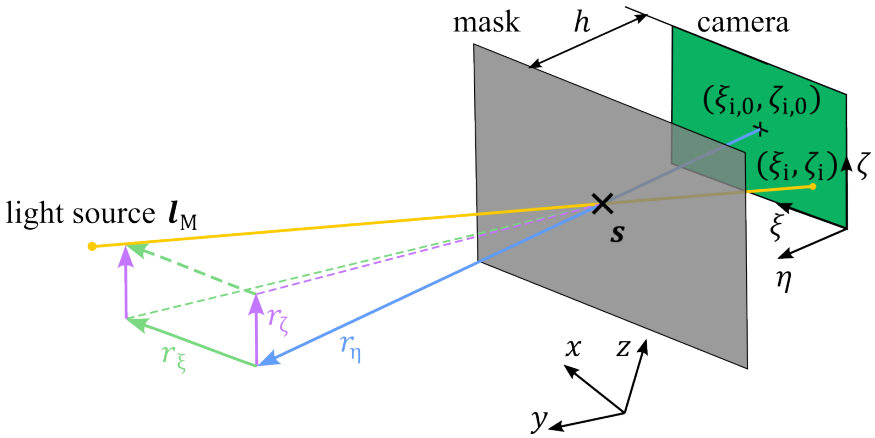

Fig. 1. Shadow imaging principle for each sensor. The sensor index n is omitted here. The light source at its position $\boldsymbol{l}_M$ casts the mask's shadow onto a camera chip. The shadow position (ξ_i, ζ_i) in the (ξ, ζ)-image plane is where the shadow of the mask center $\boldsymbol{s}$, denoted by a black cross, is observed. The vector components r_ξ, r_η and r_ζ in sensor coordinates give the direction to the light source.

Tool pose measurement.

To obtain the tool pose, the separate measurement of three light source positions is necessary. To distinguish the signals during the measurement and avoid overlapping shadows, light sources with different wavelength are used in this article which is feasible in single shot measurements and for various tool orientations.

The tool pose is described by the tool position $\boldsymbol{p}_0$, and the tool orientation is defined by the Euler-angles $(\alpha_T, \beta_T, \gamma_T)$. Thereby, the Euler-angles form the rotation matrix $\boldsymbol{R}_{MT}$ so that each position $\boldsymbol{l}_{T,k}$ of a light source $k = 1 \dots K$ in tool coordinates known from a calibration is expressed in machine coordinates as follows:

$$\boldsymbol{l}_{M,k} = \boldsymbol{R}_{MT} \cdot \boldsymbol{l}_{T,k} + \boldsymbol{p}_0. \tag{4}$$

Since the light source position $\boldsymbol{l}_{M,k}$ in machine coordinates is measured by the shadow imaging sensors, subtracting the $(k+1)$-th light source position from the k-th

$$(\boldsymbol{l}_{M,k} - \boldsymbol{l}_{M,k+1}) = \boldsymbol{R}_{MT} \cdot (\boldsymbol{l}_{T,k} - \boldsymbol{l}_{T,k-1}) \tag{5}$$

eliminates the tool position and enables solving for the rotation matrix $\boldsymbol{R}_{MT}$ using at least three light sources. The elements r_{uv} in the rotation matrix provide the tool orientation angles

$$\alpha_T = \operatorname{atan2}(r_{23}, r_{33}); \quad \beta_T = \operatorname{atan2}\left(-r_{13}, \sqrt{{r_{23}}^2 + {r_{33}}^2}\right); \quad \gamma_T = \operatorname{atan2}(r_{12}, r_{11}). \tag{6}$$

Utilizing the determined rotation matrix $\boldsymbol{R}_{MT}$ and solving Eq. (4) for $\boldsymbol{p}_0$, each light source contributes an estimate for calculating the tool position

$$\boldsymbol{p_0} = \frac{1}{K} \cdot \left(\sum_{k=1}^{K} (\boldsymbol{l}_{M,k} - \boldsymbol{R}_{MT} \cdot \boldsymbol{l}_{T,k})\right) \tag{7}$$

as the average of the result of the K light sources.

Method

Shadow imaging sensor.

The basic shadow imaging sensor consists of a DMM 37UX273-ML monochrome board camera and a mask located 20 mm in front of the camera chip, and the light source is realized by any surface-mounted device LED type 0805. The camera resolution is 1440 px × 1080 px with a pixel size of 3.45 µm. The mask shown in Fig. 2 comprises vertical and horizontal grid segments that are alternately arranged, and each orientation provides one component of the shadow position. Each grid segment is 2.0 mm × 1.5 mm with 100 µm wide stripes so that continuous visibility of at least one grid is ensured. The inclusion of 8-bit binary codes in the initial transparent stripe creates an index for each grid, aiding in determining its position relative to the mask center.

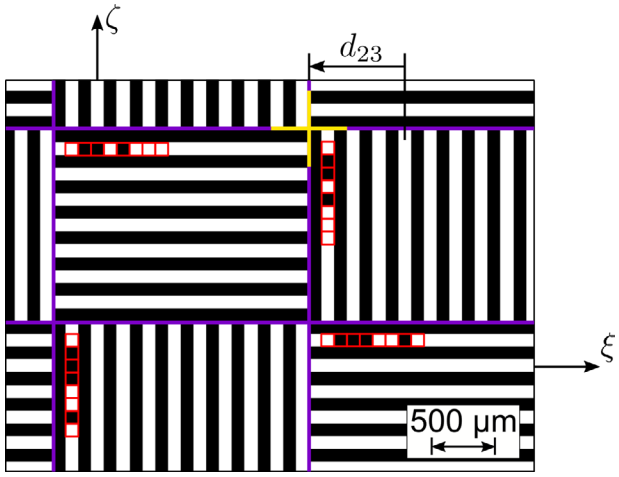

Fig. 2. Mask cutout for the shadow imaging sensors with opaque (black) and transparent (white) parts. Grid borders are marked by purple lines and the mask center is shown by the yellow cross. Red squares denote code bits of the grid segment index. The shown axes ξ and ζ are on the camera plane whereas the distance d_a between the mask center and the stripe a, exemplarily indicated for the stripe $a = 23$, is known in the mask plane.

To calculate the direction vector to an LED from a captured image, the shadow position must be evaluated in the image, which is explained in detail in [10]. Here, it is assumed, that the LED light is sufficiently distinguished so that the image processing is robust against interfering LEDs. During image processing, the alternately arranged grid segments are separated first. Then, the stripes per grid are localized by approximating a limited gaussian function to the smoothened intensity profile of each bright stripe. Thus, the peak position μ_a is calculated for each stripe a that serves as stripe location in the camera plane. For calculating the absolute shadow position, the mask's stripe coordinates relative to its center are derived using the index of a grid segment in the image. To determine the horizontal shadow position ξ_i, an estimate

$$\xi_{\mathrm{i},a} = \mu_a + d_a \cdot f \tag{9}$$

is calculated for each vertical stripe a from the stripe location μ_a, the horizontal mask coordinate d_a of the stripe and the magnification f of the image, i. e. the factor between mask features and corresponding shadow features, and the estimates are averaged afterwards. Respectively, for the vertical shadow position ζ_i, horizontal stripes provide shadow position estimates. Thus, the shadow position $(\xi_\mathrm{i}, \zeta_\mathrm{i})$ is obtained by means of processing the shadow images, and the direction vector to the LED can be calculated.

Experimental setups.

The position measurement uncertainty for a single LED is examined using a minimal setup with three shadow imaging sensors, as presented in Fig. 3a. The uncertainty is investigated in the measuring volume of sensor 1 at position (0 mm, 0 mm, 0 mm) with a y-range (axial) of 500 mm, an x-range (horizontal lateral) of 300 mm and a z-range (vertical lateral) of 200 mm. This volume begins at a distance of 300 mm in front of sensor 1 and is divided into two sub-regions, where sensor 2 at (-550 mm, 425 mm, 0 mm) and sensor 3 at (-550 mm, 675 mm, 0 mm) are utilized for triangulation, respectively. The green LED (WENGN02-C1M) listed in Table 1 is directed in a - 45° angle so that it is visible from both sensor perspectives.

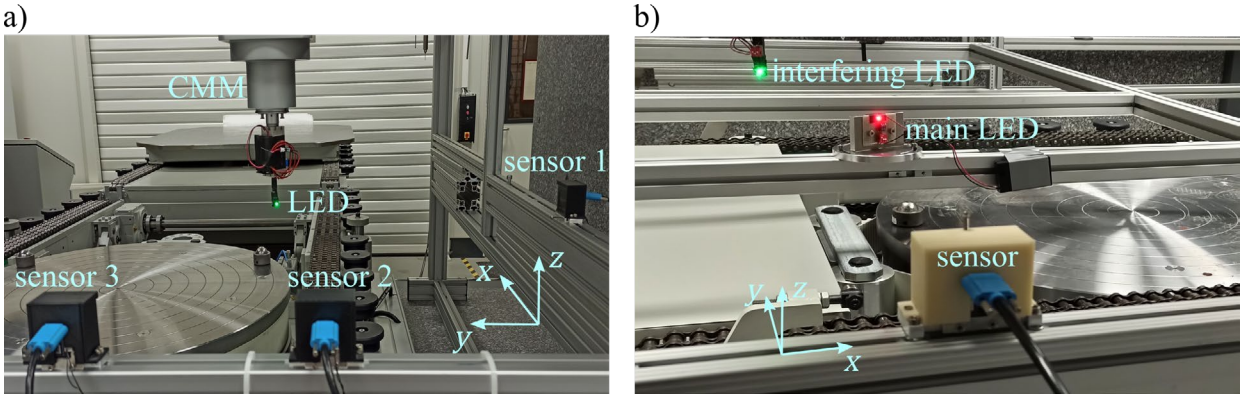

Fig. 3. Setups used for experimental investigation of the the LED position measuring uncertainty contribution. a) Examination of the systematic and random error in measuring the 3D position of a single LED in a volume of 500 mm × 300 mm × 200 mm. b) Setup to reveal cross-sensitivities between two LEDs.

When the experiment is conducted, a coordinate measuring machine (CMM) Leitz PMM-F 30.20.7 positions the LED and at every location, the sensors capture ten images with an exposure time of 25 ms and a reference position is provided by the CMM. After calibration, the LED is repositioned across multiple points with a distance of 10 mm along each axis to analyze both systematic and random errors.

The cross-sensitivities between LEDs with different wavelength are investigated using a second setup where a red, a green and an ultraviolet (UV) LED is used. Here, according to Fig. 3b, only one sensor but two LEDs are used and a color filter is positioned in front of the camera that is transmissive for only one LED, the main LED, while the second LED is interfering the image data. The LEDs and the corresponding filter configurations are given in Table 1.

Table 1. LEDs used for cross-sensitivity investigation and filter configurations applied to transmit the respective LED light.

LED			**filter configuration**
name	**wavelength [nm]**	**beam angle [°]**	**description**
WENUV1-CM	421 (ultraviolet)	120	color glass BG3 (Schott) & color film in magenta
WENGN02-C1M	520 (green)	140	color glass VG9 (Schott) & color film in green
WENRD09-C1M	625 (red)	140	color film in red

For the experiment, it is assumed that a tool holder with a diameter of 150 mm is used and that the LEDs are positioned every 60° on the surface. Thus, an average condition with two adjacent LEDs oriented in angles of +30° and -30° is represented in the experiment. The main LED is on a fixed position in a measuring distance of 500 m and a lateral position of 37.5 mm from the center.

The interfering LED is moved stepwise by the CMM along the x-axis in a range of -100 mm to +100 mm with respect to the main. In vertical direction, the distance between the LEDs is 37.5 mm which leads to a vertical shift between the shadows of both LEDs of one grid height. During the movement ten images are recorded every 0.5 mm with an exposure time of 50 ms.

Monte Carlo simulation.

To estimate the tool pose measurement uncertainty, a Monte Carlo simulation is applied. Initially, the tool position and orientation in the MCS, and three true LED positions in the tool coordinate system on the tool holder at alternating heights of 0 mm and 100 mm are defined. Then, the LED positions are transformed into the MCS, and the simulated LED position measurement error is added to each true LED position. The tool pose error is calculated for 10000 sets of simulated LED position measurements to enable a proper statistical evaluation. The procedure is repeated for 1000 random tool poses, whereby the tool positions are spread over the entire measurement volume and the orientation is in a range of $\pm$ 45° for α_T and β_T, and of $\pm$ 30° for γ_T.

To simulate the LED position measurement error, contributions to the uncertainty, systematic and random errors in single LED measurement, and cross-sensitivity between LEDs, are integrated based on their statistical distribution across the measuring volume. The systematic error is composed of a predictable tendential course and an unpredictable scatter. The scattering error is determined on multiple paths in the measurement volume and a standard deviation of all error values is calculated. The random error's standard deviation is the propagation of a fluctuating shadow position which depends on the angle of view and is modelled from the experimental results. Thus, the random measurement error is generated from the standard deviation that corresponds to a random position in the measurement volume. Regarding the cross-sensitivity, the experimentally detected LED position measurement error is used to assess the standard deviation of the shadow position, which is propagated to a random position in the measuring volume. Here, only the effect of the interfering LED leading to the major error is considered.

Results

Systematic error.

The systematic error is evaluated using the three-sensor-setup by calculating the error between the average measured position and the reference position. The observation of the systematic error $\Delta(x_\mathrm{L})$, mainly affected by sensor 1, is presented in Fig. 4a and shows a strong parabolic course overlaid by a scatter that is increasing to larger angles of view. The parabolic course is predictable, so the scatter of the systematic error $\Delta(x_\mathrm{L})$ caused by varying magnification values is evaluated on paths along the z-axis. The frequency distribution of the remaining scattering error $\Delta_\mathrm{c}(x_\mathrm{L})$ on all paths, shown in Fig. 4b, follows a normal distribution with a standard deviation of 33 µm. Accordingly, the scatters of the systematic errors $\Delta(y_\mathrm{L})$ and $\Delta(z_\mathrm{L})$, also included in Fig. 4b, are extracted on paths along the z- and x-axis which leads to standard deviations of 29 µm and 25 µm, respectively. Therefore, the systematic scatter is more than the half of the allowed tool position uncertainty.

Random error.

The random LED position measurement error is evaluated based on the three-sensor-setup as the standard deviation of the evaluated LED positions. Fig. 5a shows the standard deviation of the measured x_L-LED position component along the x-axis at $z_\mathrm{L,ref} = 0$ mm. The standard deviation $\sigma(x_\mathrm{L})$ increases with the angle of view between sensor 1 and the $x_\mathrm{L,ref}$ position component. The strong angle-dependent increase is primarily caused by the propagation of the magnification uncertainty $u(f)$ to the shadow position component ξ_i of sensor 1, see Eq. 9. As a result, the $z_\mathrm{L,ref}$ position component has hardly any influence on the standard deviation $\sigma(x_\mathrm{L})$. The secondary effect is the increase of the LED position standard deviation $\sigma(x_\mathrm{L})$ with the axial distance $y_\mathrm{L,ref}$. Assuming the ideal sensor setup as described previously, including that the rotation

matrix $\boldsymbol{R}_{\mathrm{MS},1}$ is a zero matrix and that the uncertainty of the y_{L} component is negligible, the uncertainty

$$u(x_{\mathrm{L}}) = u(\xi_{\mathrm{i}}) \cdot \frac{y_{\mathrm{L,ref}}}{h} \tag{10}$$

is the shadow position uncertainty $u(\xi_{\mathrm{i}})$ scaled by the relation between the axial distance $y_{\mathrm{L,ref}}$ and the distance h between mask and camera. The standard deviations $\sigma(y_{\mathrm{L}})$ and $\sigma(z_{\mathrm{L}})$ show an according course, but the standard deviations are slightly smaller for the y_{L}-component because the angle of view is smaller, and the standard deviations are particularly small for the z_{L}-component since the information provided by two perspectives is averaged.

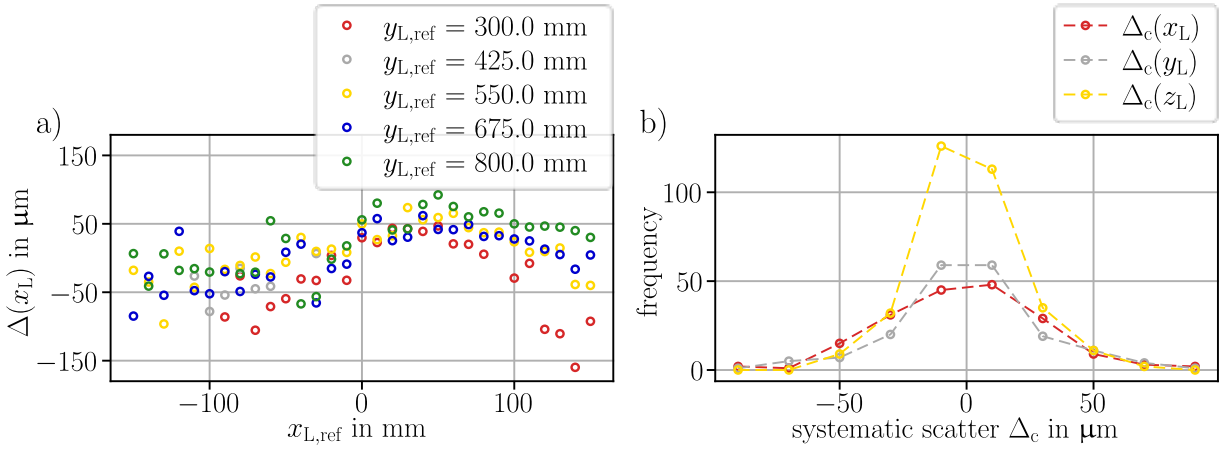

Fig. 4. Systematic error of the measured LED position. a) Systematic error $\Delta(x_{\mathrm{L}})$ evaluated on paths along the x-axis vertically centered in front of sensor 1. b) Frequency distribution of the systematic error values after the correction of the tendential course.

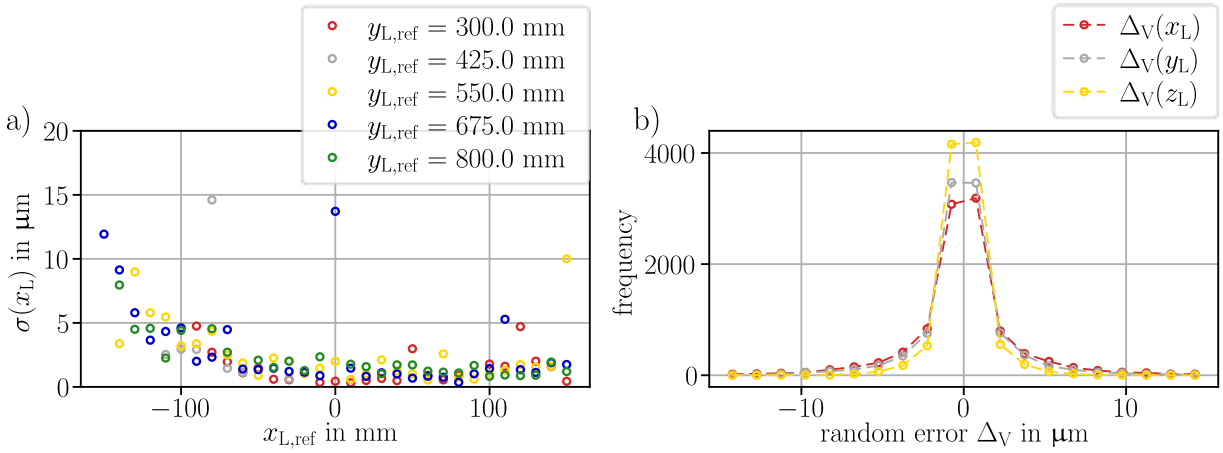

Fig. 5. Random error of the LED position. a) Standard deviation of the measured LED position component x_L evaluated on paths along the x-axis at $z_{L,ref} = 0$ mm. b) Frequency distribution of 10000 simulated random error values Δ_V following the empirical model.

For establishing an empirical model for the position dependent random error, the LED position standard deviation $u(x_{\mathrm{L}})$ is extracted on the path at $y_{\mathrm{L,ref}} = 675$ mm, which is centered in front of sensor 3, rescaled to the shadow position standard deviation and approximated by a parabola in dependence of the angle of view. The same empirical model is applied for the y_{L}- and z_{L}-

component, but the respective lateral and axial LED position components for Eq. 10 are adapted to the laterally measuring sensor. Since the z_L-component is covered from both sensor perspectives, both respective sensors provide a random error that is averaged then.

To further investigate the statistical distribution of the random error in the entire measuring volume, uniformly distributed positions are generated and random error values Δ_V that follow a normal distribution with the model-based standard deviation are simulated. After 10000 simulations, the frequency distribution of random errors Δ_V shown in Fig. 5b results. The standard deviation $\sigma(\Delta_V(x_L))$ of random error values of the LED position component x_L in the entire measuring volume is 3.5 µm, and for the y_L- and z_L-component, the standard deviation is $\sigma(\Delta_V(y_L)) = 2.7$ µm and $\sigma(\Delta_V(z_L)) = 1.4$ µm.

Cross-sensitivities.

Experiments with the setup shown in Fig. 3b provide an estimation on the cross-sensitivities between LEDs of different colors. The main LED position component $x_{L,main}$ is evaluated from the shadow position component ξ_i assuming $x_{L,main} = 0$ mm as mean position, an ideal sensor setup and involving the axial position $y_{L,ref}$ from the CMM. The deviations of the mean main LED position per position of the interfering LED, presented in Fig. 6 for all combinations of LEDs, show that the deviation remains below 15 µm which is promising for tool pose measurement.

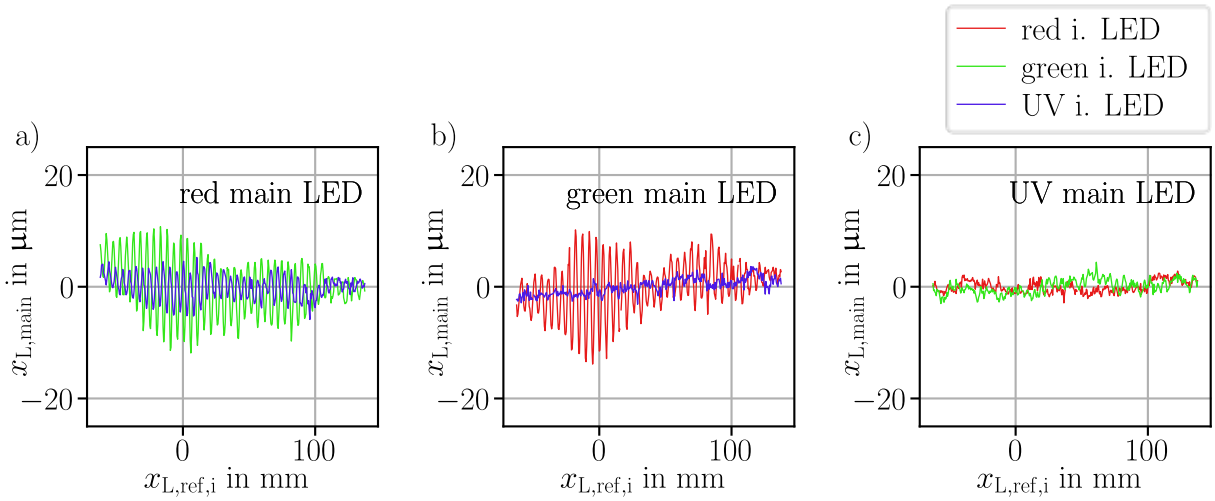

Fig. 6. Measured lateral positions of fixed main LEDs while an interfering LED is moved above the main LED. The deviation of the main LED position $x_{L,main}$ is the error due to cross-sensitivities between the LEDs. a) Red main LED, b) green main LED, c) UV main LED.

Furthermore, for the red main LED shown in Fig. 6a, a periodic course of the main LED position is present for both interfering LEDs. This periodicity occurs due to slight transmissivity of the color filter for the interfering light, causing the shadows of both LEDs to superpose. Two slightly shifted overlapping stripe shadows result in a shifted stripe shadow position and thus a shifted measured LED position. For the green interfering LED, the shift of the main LED $x_{L,main}$ varies also in the amplitude as the interfering LED moves. The amplitude increases with a larger overlap between vertical grid segment shadows and a higher intensity of the interfering shadow.

The error due to cross-sensitivities is normally distributed along the captured path. For the red main LED, the green interfering LED leads to the higher error with a standard deviation of 6.5 µm. While the red LED interferes the measurement of the green main LED in a distinct periodic course with a total standard deviation of 5.2 µm, the UV LED movement results in a low noisy error, see Fig. 6b. The cross-sensitivity error of the UV main LED shown in Fig. 6c is barely detectable with a standard deviation of 2.0 µm for the green interfering LED while the red interfering LED has a

minor influence. It is assumed that the vertical position component is affected accordingly. However, the cause of the LED position error is the shadow position error so that the position error will increase with an increasing axial distance between sensor and LED.

Tool pose measurement.

To assess the feasibility for tool pose measurement using shadow imaging, the revealed uncertainty contributions are combined by means of a Monte Carlo simulation. In summary, the systematic scatter contributes the strongest to the LED position measurement uncertainty, followed by the error due to cross-sensitivities, and the random error has the lowest impact.

The frequency distribution of the resulting tool position and orientation measurement error is shown in Fig. 7a and Fig. 7b, respectively, for one exemplary tool pose. It is evident that the majority of the position errors is in the allowed range of $\pm$ 50 µm and also the orientation error is mostly in the required range of $\pm$ 0.05°. In fact, over all 1000 tool poses, at least 92 % of the simulated error values per position or orientation component are within the required range.

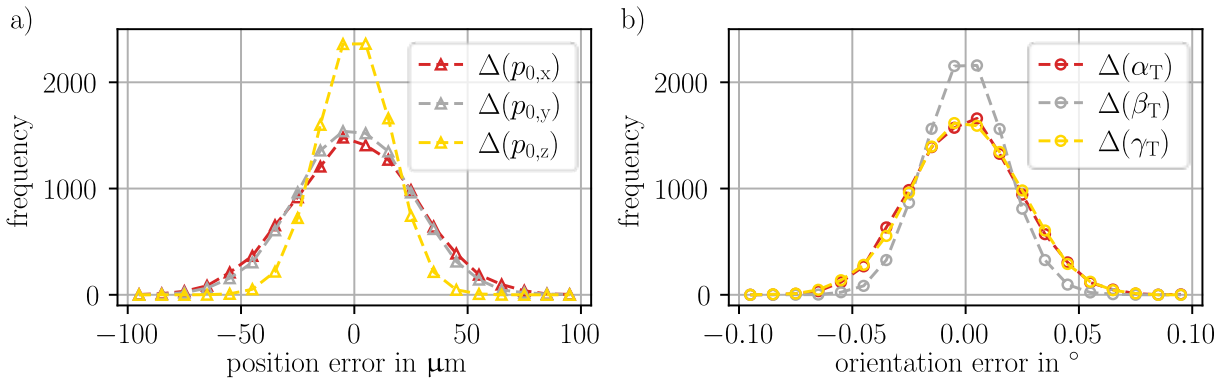

Fig. 7. Frequency distributions of 10000 tool pose errors applied to one exemplary tool pose, divided in the respective a) tool position components ($p_{0,x}$, $p_{0,y}$, $p_{0,z}$) and b) tool orientation components (α_T, β_T, γ_T).

Furthermore, the results show that the tool position component $p_{0,x}$ has the highest uncertainty. The reason for this is that the LED position measurement uncertainty of the x_L-component is the highest while the tool orientation range is limited. Even the root of the mean squared error (RMSE), calculated for all simulated tool poses is the highest for the tool position component $p_{0,x}$ with 26 µm, while the RMSEs of the components $p_{0,y}$ and $p_{0,z}$ are each 21 µm on average. The frequency distribution of the tool orientation error demonstrates that the error of the component β_T has the lowest uncertainty which is confirmed by the other tool poses. The average RMSE is 0.017° while the components α_T and γ_T both show an average RSME of 0.021°.

In conclusion, the results of the Monte Carlo simulations show that tool pose measurement using shadow imaging is feasible with the required measuring uncertainty since the majority of the simulated tool position and orientation errors is in the aimed uncertainty range and the evaluated RMSEs are around the half of the required measuring uncertainty.

Summary

To achieve a position and orientation measurement uncertainty of 50 µm and 0.05°, respectively, required for tool pose measurement during ISF, a triangulation system based on shadow imaging sensors measuring positions of LEDs attached to the tool holder, is introduced. The contributions to LED position measurement uncertainty, including cross-sensitivities between different LEDs, are examined. To finally assess the feasibility of tool pose measurement, the tool pose error resulting from the LED position uncertainty was investigated applying a Monte Carlo simulation.

The Monte Carlo simulation revealed that shadow imaging sensors are capable of measuring the tool pose with a sufficient measurement uncertainty. From the experimental results on the contributions to the LED position uncertainty, it stands out that the scatter in the systematic error resulting from variations in the evaluated magnification primarily influences the uncertainty budget, and that the lowest contribution is the random error caused by image noise. The effect of cross-sensitivities is reduced to a sufficient level, comparable to the random error, by applying the respective color filters.

Although the Monte Carlo simulation proved the feasibility of measuring the tool pose with the proposed measuring principle, an experimental validation is still pending and will be subject of future work. Furthermore, the reduction of the measurement duration and the processing time, to demonstrate the capability of real-time tool pose measurement, will be covered in further studies.

References

[1] W. Ji, L. Wang: Industrial robotic machining: a review. Int J Adv Manuf Technol 103(1-4):1239–1255, 2019. https://doi.org/10.1007/s00170-019-03403-z

[2] H. Zu, X. Chen, Z. Chen, Z. Wang, X. Zhang: Positioning accuracy improvement method of industrial robot based on laser tracking measurement. Measurement: Sensors 18:100235, 2021. https://doi.org/10.1016/j.measen.2021.100235

[3] G. Xiong, Z.-L. Li, Y. Ding, L. Zhu: A closed-loop error compensation method for robotic flank milling. Robotics and Computer-Integrated Manufacturing 63:101928, 2020. https://doi.org/10.1016/j.rcim.2019.101928

[4] A. Nubiola, I. A. Bonev: Absolute calibration of an ABB IRB 1600 robot using a laser tracker. Robotics and Computer-Integrated Manufacturing 29(1):236–245, 2013. https://doi.org/10.1016/j.rcim.2012.06.004

[5] T. Shu, S. Gharaaty, W. Xie, A. Joubair, I. A. Bonev: Dynamic path tracking of industrial robots with high accuracy using photogrammetry sensor. IEEE/ASME Trans. Mechatron. 23(3):1159–1170, 2018. https://doi.org/10.1109/TMECH.2018.2821600

[6] J. Tang, T. Zhou, E. Zakeri, T. Shu, W.-F. Xie: Photogrammetry-based Dynamic Path Tracking of Industrial Robots Using Adaptive Neuro-PID Control Method and Robust Kalman Filter. 2023 9th International Conference on Automation, Robotics and Applications (ICARA), Abu Dhabi, United Arab Emirates, 10.02.2023 - 12.02.2023. https://doi.org/10.1109/ICARA56516.2023.10125681

[7] J. Lin, Y. Li, Y. Xie, J. Hu, J. Min: Joint stiffness identification of industrial serial robots using 3D digital image correlation techniques. Proceedings of the Institution of Mechanical Engineers, Part C: Journal of Mechanical Engineering Science 236(1):536–551, 2022. https://doi.org/10.1177/09544062211002878

[8] T. Luhmann: Close range photogrammetry for industrial applications. ISPRS Journal of Photogrammetry and Remote Sensing 65(6):558–569, 2010. https://doi.org/10.1016/j.isprsjprs.2010.06.003

[9] E. Grenet, P. Masa, E. Franzi, D. Hasler: Measurement system of a light source in space 14.07.2011

[10] M. Terlau, A. von Freyberg, D. Stöbener, A. Fischer: Shadow-Imaging-Based Triangulation Approach for Tool Deflection Measurement. Sensors (Basel) 23(20):2023. https://doi.org/10.3390/s23208593